Engineering of Mixed Eu 3+ /Tb 3+ Metal-Organic Frameworks Luminescent Thermometers with Tunable Sensitivity

Virgile Trannoy, Albano Carneiro Neto, Carlos Brites, Luís Carlos, Hélène Serier-brault

Engineering of mixed Eu^{3+}/Tb^{3+} metal-organic frameworks luminescent thermometers with tunable sensitivity

Virgile Trannoy, Albano N. Carneiro Neto, Carlos D. S. Brites, Luís D. Carlos, Hélène Serier-Brault**

((Optional Dedication))

Dr. V. Trannoy, Dr. H. Serier-Brault
Université de Nantes, CNRS, Institut des Matériaux Jean Rouxel, IMN, F-44000 Nantes, France
E-mail: helene.brault@cnrs-imn.fr

Dr. A. N. Carneiro, Neto, Dr. C. D. S. Brites, Pr. L. D. Carlos
Phantom-g, CICECO – Aveiro Institute of Materials, Department of Physics, University of Aveiro, 3810-193 – Aveiro, Portugal
E-mail: lcarlos@ua.pt

Keywords: metal-organic frameworks, luminescent thermometers, europium, terbium, Tb-to-Eu energy transfer

Abstract

In the last decade, numerous Ln-bearing metal-organic frameworks are reported for luminescence thermometry applications. Although its Ln^{3+} composition is always thoroughly determined, this parameter is never optimized to improve thermometric performances. Here, we tackle the optimization of thermometric performances of luminescent probes by reporting a series of mixed Eu^{3+}-Tb^{3+} metal-organic frameworks. The thermometric performances are accessed as a function of the Eu^{3+} content yielding to a maximum relative sensitivity between 0.19 and 0.44 $\%\cdot K^{-1}$ registered at temperatures between 340 and 240 K, respectively. A meticulous theoretical investigation of the Tb^{3+}-to-Eu^{3+} energy transfer in the series of mixed Eu^{3+}-Tb^{3+} metal-organic frameworks is also performed to determine the predominant pathway of the energy transfer. For the first time, we present clear evidence the significant influence of the Eu/Tb ratio on the energy transfer between Ln^{3+} emitting centers that definitively determines the operating temperature range and the maximum relative sensitivity of the luminescent thermal probes.

1. Introduction

Metal-Organic Frameworks (MOFs) are crystalline porous materials built up from metallic nodes and organic linkers that have attracted great interest due to their wide range of possible applications.[1–5] Effectively, the wide variety of chemical composition, structural diversity, conjugated with its intrinsic adjustable porosity makes these materials promising candidates not only for purely sorption-related applications but also in other areas where their tunable optical or electronic properties can be exploited for diverse applications.[6–9] The lanthanide-bearing MOFs (Ln-MOFs) is a sub-class of MOFs whose optical properties may arise either from the organic or from the inorganic part, have emerged as unique and promising luminescent thermometers.[10–17] Indeed, compared to conventional contact thermometry, luminescent thermometry have unique and distinct advantages of fast response, high accuracy, being non-invasive and presenting high spatial resolution (typically submicron scale) where traditional methods are ineffective.[18–20] Among the diverse aspects to Ln^{3+}-based luminescent thermometry, one of the most robust methodologies relies on the measurement of the intensity of two transitions of distinct Ln^{3+} emitting centers. For mixed-metal Ln-MOFs, the temperature is most often determined from the ratio between the intensity of the $^5D_4 \rightarrow {}^7F_5$ and of the $^5D_0 \rightarrow {}^7F_2$ transitions of Tb^{3+} and Eu^{3+}, respectively.[15,21,22]

Since the first report of the ratiometric Eu-Tb-mixed MOF luminescent thermometer,[21] the number of materials displaying potential for luminescent thermometry increased drastically, notably because of the inexhaustible selection of suitable organic ligands. However, not many works have been devoted to identifying the structural parameters which can govern the fine-tuning of the thermometric performance parameters, namely the operating temperature range and the relative thermal sensitivity. Recently we investigated the thermometric properties of an Eu-Tb mixed MOF built upon the bidentate linker 1,3-benzene-dicarboxylic acid (1,3-H_2bdc, also called isophthalic acid), namely $[Tb_{0.87}Eu_{0.13}(1,3\text{-bdc})_3(H_2O)_2]$, presenting the maximum

relative thermal sensitivity in the cryogenic range (T<100K).[23] The 1,3-H_2bdc linker is a bidentate ligand with different geometric effects to connect metal ions into multidimensional structures *via* numerous coordination modes. Consequently, several MOFs based on this ligand have been already reported with different structuration, despite their thermometric performance have not always been studied.[24–28]

Herein we reported the study of another Eu-Tb mixed isophthalate MOF, [$Tb_{1-x}Eu_x(CH_3COO)$(1,3-bdc)(H_2O)], using isophthalic acid as the linker, which contains Ln_2 SBUs as inorganic nodes in a 3D framework and with an ancillary ligand.[24–26] Aiming at the rational design of the operating temperature range and relative thermal sensitivity of isophthalate MOFs, we investigated the luminescence properties of a series of six distinct Eu-Tb compositions (the Eu^{3+} content varying from 3 to 15 mol.%). To gain some rational on the design of these intriguing samples, we use theoretical simulations of the Tb^{3+}-to-Eu^{3+} energy transfer for correlating the chemical composition with the thermometric properties and determine what is the main Tb^{3+}-to-Eu^{3+} energy transfer pathway which is determinant for the rational engineering of the compounds looking forward to fine-tuning of the maximum relative sensitivity and the corresponding temperature at which it occurs.

2. Structural and chemical characterization

Three single-doped compounds, Ln-CP (Ln=Eu, Tb, or Gd) were obtained in moderate yields as a white microcrystalline powder using hydrothermal conditions. The powder X-ray diffraction (PXRD) analysis (Figure S1) and FTIR measurements (Figure S2) reveal all coordination polymers are isostructural with the Ln(Ac)(ip)(H_2O)$_2$·0.5H_2O compounds (Ln=Gd, Sm, Nd, Sm, Eu, La) reported in the literature.[24–26] The asymmetric unit is composed of symmetric dimers of Eu^{3+} cations, six 1,3-bdc^{2-} ligands, two acetate ligands, and four coordinated water molecules (**Figure 1a,b**). Each Ln^{3+} is 9-coordinated in tricapped trigonal

prismatic geometry formed by nine O-atoms from three different 1,3-bdc^{2-} ligands, two distinct acetate ligands, and two water molecules. Both [LnO_9] polyhedra are bridged by two acetate O-atoms to generate the Ln_2 SBU of an edge-sharing polyhedron, where the Ln-Ln distance is 4.35 Å in a dimer. Each dimer is also connected to six 1,3-bdc^{2-} ligands, playing the role of the organic spacer with other neighboring dimers to generate a three-dimensional coordination polymer, the smallest Ln-Ln distance between two Ln_2 SBU units is 5.78 Å. The thermal (Figure S3) and elemental analyses confirmed the chemical composition of single doped compounds.

The mixed compounds denoted by $Tb_{1-x}Eu_x$ (x = 0.030, 0.050, 0.075, 0.100, 0.125, and 0.150, the obtained molar ratio was determined by ICP-AES, Table 1S) were obtained pure in moderate yields as a white microcrystalline powder. Both PXRD analysis (**Figure 1c**) and FT-IR spectroscopy (Figure S4) confirm that the mixed compounds are isostructural with the pure compounds.

3. Photophysical properties

The luminescence properties were investigated in the solid-state at room temperature. Upon excitation at 289 nm, the emission spectra of Tb-CP (Figure S5) and Eu-CP (Figure S6) display the characteristic green and red luminescence of Tb^{3+} and Eu^{3+} ions, respectively, exhibiting typical lines at 488, 542, 585 and 619 nm, for Tb-CP, and at 582, 616, 650 and 692 nm, for Eu-CP. The emission lines are attributed to the Tb^{3+} $^5D_4 \rightarrow {}^7F_{6-3}$ transitions and the Eu^{3+} $^5D_0 \rightarrow {}^7F_{1-4}$ transitions, respectively. Furthermore, the emission bands of the 1,3-bdc^{2-} ligand are completely absent in the luminescent spectra of both compounds, evidencing an efficient sensitization of both Tb^{3+} and Eu^{3+} ions by the organic ligand. The phosphorescence spectrum at 77 K (Figure S7) of Gd-CP was recorded to identify the lowest-lying triplet energy state positioning of the organic ligands. Then, the triplet level is estimated to be 26040 cm^{-1} from the shortest-

wavelength, which is in a suitable energy range to sensitize both Eu^{3+} and Tb^{3+} according to the Latva's empirical rule.[29]

The emission spectra of the mixed compounds exhibit the intra-4f transitions of the Tb^{3+} and Eu^{3+} ions (Figure S8). Increasing the Eu^{3+} content the emission color shifts for x = 0.030, pure green emission (similar to that of the Tb-CP compound), to essentially pure red when x = 0.150 (as registered for the Eu-CP), (Figure S9 and Table S2). This shift in the color coordinates is due to the Tb^{3+}-to-Eu^{3+} energy transfer, which was evidenced by the presence of $^7F_6 \rightarrow {}^5D_4$ Tb^{3+} transition (at 483 nm) within the $^5D_0 \rightarrow {}^7F_2$ Eu^{3+} transition in the excitation spectra of a mixed compound (Figure S10).

The $^5D_4$ (monitored at 545 nm) and $^5D_0$ (monitored at 615 nm) decay curves of single-doped and codoped samples are well described by single exponential functions, (Figure S11 to S13). In the mixed compounds, the Tb^{3+}-to-Eu^{3+} energy transfer rate (W_{exp}) and the transfer efficiency (η_{ET}) were determined from Equation 1 and 2, respectively:[30–33]

$$W_{\text{exp}} = \frac{1}{\tau} - \frac{1}{\tau_0} \qquad (1)$$

$$\eta_{ET} = 1 - \frac{\tau}{\tau_0} \qquad (2)$$

where τ and τ_0 correspond to the lifetimes of the donor (Tb^{3+}) in the presence and absence of the acceptor (Eu^{3+}), respectively (Table S3 to S5 and **Table 1**). The obtained values are reported in Table 1 and Figure S14. Then, as suggested by the rapid evolution of CIE coordinates with the increase of Eu^{3+} (Figure S9), the Tb^{3+}-to-Eu^{3+} energy transfer is relatively high and varies from 77%, for x = 0.030, to 93%, for x = 0.150 (Figure S15).

4. Luminescent thermometry

The temperature-induced change on the emission spectrum motivated the application of the mixed compounds for luminescent thermometry. As an illustrative example, **Figure 2a** presents the temperature-dependent emission spectra of the compound with x = 0.150 in the 150–350 K range (similar data of all the other mixed compounds are reported in Figure S16 to S20). The integrated areas of the $^5D_4 \rightarrow {}^7F_5$ (Tb^{3+}), I_1, and $^5D_0 \rightarrow {}^7F_2$ (Eu^{3+}), I_2, transitions were calculated in the 530–560 nm and 603–633 nm ranges, respectively. As five consecutive emission spectra were recorded for each sample and each temperature, the mean values of the areas ± SD were reported. While I_1 corresponds to only the $^5D_4 \rightarrow {}^7F_5$ transition (the $^5D_1$ Eu^{3+} emission is not discerned, Figure S6 and S21), the I_2 integration range includes a small (ca. 6%) contribution from the Tb^{3+} $^5D_4 \rightarrow {}^7F_3$ transition (Figure S21). The contribution of the Eu^{3+} emission to I_2 is, thus, highly dominant (>93%) and both $I_2(T)$ and the thermometer performance is unaffected by the presence of the $^5D_4 \rightarrow {}^7F_3$ transition (Figure S22). This is valid for all the Tb^{3+} contents studied in this work and, therefore, in what follows we consider the commonly assumed labelling of I_2 as being only due to the $^5D_0 \rightarrow {}^7F_2$ contribution.

The integrated areas of the transitions originated in both Ln^{3+} centers present a clear thermal quenching (**Figure 2b**) compared to the thermal quenching present in the ***Tb-CP*** and ***Eu-CP*** (Figure S11 and S12). Whereas I_2 decreases about 10% of its initial value, I_1 decreases almost 50% upon temperature increase (the same is valid for all the other samples). As the temperature dependence of the I_1 is much higher than that of I_2, we consider that the temperature dependence of the I_1/I_2 ratio is determined essentially by the thermal quenching of the Tb^{3+} transition (I_1). We use the phenomenological Mott-Seitz expression for a single deactivation channel to describe the $I_1(T)$ dependence:[34,35]

$$I_1(T) = \frac{I_{01}}{1 + \alpha \exp(-\Delta E / k_B T)} \qquad (3)$$

where I_{01} is the integrated area in the limit of $T \rightarrow 0$ K, α is the ratio between the nonradiative and radiative decay rates in the limit of $T \rightarrow 0$ K, and ΔE is the energy difference between the emitting level ($^5D_4$) and the level responsible for its nonradiative deactivation. The ratio between the integrated areas of the I_1 and I_2 transitions is thus described by:[14]

$$\Delta \equiv \frac{I_1}{I_2} \approx \frac{\Delta_0}{1 + \alpha \exp(-\Delta E / k_B T)} \qquad (4)$$

where Δ_0 is the I_1/I_2 ratio in the limit $T \rightarrow 0$ ($\Delta_0 = I_1/I_{02}$). Fitting Equation 4 to the experimental $\Delta(T)$ curves we find excellent correlation coefficients attesting the adequacy of this simple model to get the calibration curve of the mixed compounds (Figure S23). The fitting parameters for the $Tb_{1-x}Eu_x$ compounds are listed in **Table 2** and show a decrease of ΔE and an increase of α as the Eu content increases (**Figure 2d**). As the Tb^{3+}-to-Eu^{3+} energy transfer efficiency is independent of the temperature (Figure S14), we suggest that the quenching of the Tb^{3+} and Eu^{3+} emission intensities as temperature increases (**Figure 2b**) is due to the activation of nonradiative channels. In the former case, Tb^{3+}-to-Eu^{3+} energy transfer is responsible for the observed temperature dependence, as addressed in the next section, whereas the small temperature dependence of the $^5D_0 \rightarrow {}^7F_2$ intensity should be related to the activation of Eu^{3+}-to-ligand states back transfer. This aspect, however, is not discussed in this manuscript.

To evaluate the thermal performance of the mixed compounds, we calculate the relative thermal sensitivity using:[14]

$$S_r = \frac{\Delta E}{k_B T^2} \left(\frac{\alpha}{\alpha + \exp(\Delta E / k_B T)} \right). \qquad (5)$$

The corresponding uncertainty (ΔS_r) is calculated using home-made MatLab® routines by propagating the uncertainty in the α and ΔE fitting parameters. Intriguingly, the increase of the Eu content on the mixed compounds influences its thermometric performance. By increasing the amount of Eu^{3+} from x = 0.030 to 0.150, a shift of 100 K towards low temperatures is observed on T_m, together with an increase in S_m from 0.19±0.02 to 0.44±0.02 %·K^{-1}. We

estimate the uncertainty in T_m determining the temperature range for which $S_r > S_m - \Delta S_r$. This variation on the relative thermal sensitivity is explained by the increase of the α and the decrease of ΔE with the increase of the Eu^{3+} content (Table 2), which means that the nonradiative rate increases relative to the radiative one, and consequently the temperature-dependence is more pronounced. These sensitivity values are comparable to the few examples existing in the literature of luminescent ratiometric MOF-based thermometers operating in the biological temperature range.[36–42] The temperature uncertainty of the thermometers is calculated using:[14]

$$\delta T = \frac{1}{S_r}\frac{\delta \Delta}{\Delta} = \frac{k_B T^2}{\Delta E}\left(\frac{\alpha + \exp(\Delta E/k_B T)}{\alpha}\right)\frac{\delta \Delta}{\Delta} \qquad (6)$$

where $\delta\Delta/\Delta$ is the relative uncertainty on the thermometric parameter, assumed as 0.1% (the minimum relative uncertainty in Δ recorded in all the samples).[14] The temperature cycling between 150 and 300 K (Figure S24) demonstrated a repeatability value higher than 99.4% at 300 K. As we will show in the next section, the dependence of S_m with the Eu^{3+} amount is well described by Tb^{3+}-to-Eu^{3+} non-radiative energy transfer processes.

5. Theoretical Tb-Eu energy transfer

In this section, it is presented a theoretical procedure to estimate the Tb-to-Eu energy transfer rates based on crystallographic structure and the theory of nonradiative energy transfer between lanthanide ions.[43,44] From the crystallographic data, one can obtain the arrangement of the host sites that can be occupied by Eu^{3+} (acceptor) or Tb^{3+} (donor) ions, as shown in **Figure 3a-c**.

The energy transfer rates between lanthanide ions were calculated taking into account the dipole-dipole (W_{d-d}), dipole–quadrupole (W_{d-q}), quadrupole–quadrupole (W_{q-q}), exchange (W_{ex}), and magnetic dipole–magnetic dipole (W_{md-md}) mechanisms,[31] Equation 7 to 11, respectively:

$$W_{d-d} = \frac{(1-\sigma_1^D)^2(1-\sigma_1^A)^2}{(2J_D^*+1)(2J_A+1)}\frac{4\pi}{3\hbar}\frac{e^4}{{R_L}^6}\left(\sum_K \Omega_K^D \langle\psi_D J_D\|U^{(K)}\|\psi_D^* J_D^*\rangle^2\right) \times\left(\sum_K \Omega_K^A \langle\psi_A^* J_A^*\|U^{(K)}\|\psi_A J_A\rangle^2\right)F \quad (7)$$

$$W_{d-q,\ q-d} = \frac{\left(1-\sigma_1^{D,A}\right)^2\left(1-\sigma_2^{A,D}\right)^2}{(2J_D^*+1)(2J_A+1)}\frac{\pi}{\hbar}\frac{e^4}{{R_L}^8}\langle f\|C^{(2)}\|f\rangle^2 \times\left[\left(\sum_K \Omega_K^D \langle\psi_D J_D\|U^{(K)}\|\psi_D^* J_D^*\rangle^2\right)\langle r^2\rangle_A^2\langle\psi_A^* J_A^*\|U^{(2)}\|\psi_A J_A\rangle^2 + \left(\sum_K \Omega_K^A \langle\psi_A J_A\|U^{(K)}\|\psi_A^* J_A^*\rangle^2\right)\langle r^2\rangle_D^2\langle\psi_D^* J_D^*\|U^{(2)}\|\psi_D J_D\rangle^2\right]F \quad (8)$$

$$W_{q-q} = \frac{(1-\sigma_2^D)^2(1-\sigma_2^A)^2}{(2J_D^*+1)(2J_A+1)}\frac{28\pi}{5\hbar}\frac{e^4}{{R_L}^{10}}\langle r^2\rangle_D^2\langle r^2\rangle_A^2\langle f\|C^{(2)}\|f\rangle^4 \times\langle\psi_D J_D\|U^{(2)}\|\psi_D^* J_D^*\rangle^2\langle\psi_A^* J_A^*\|U^{(2)}\|\psi_A J_A\rangle^2 F \quad (9)$$

$$W_{ex} = \frac{2\pi}{\hbar}\left[\left(\frac{e^2}{R_L}\right)\rho_{f-f}^2\right]^2 F \quad (10)$$

$$W_{md-md} = \frac{(1-\sigma_1^D)^2(1-\sigma_1^A)^2}{(2J_D^*+1)(2J_A+1)}\frac{4\pi}{3\hbar}\frac{{\mu_B}^4}{{R_L}^6} \times\langle\psi_D J_D\|L+2S\|\psi_D^* J_D^*\rangle^2\langle\psi_A^* J_A^*\|L+2S\|\psi_A J_A\rangle^2 F \quad (11)$$

where the intensity parameters Ω_K are obtained from Equation S1 using only the forced electric dipole (FED) mechanism (Equation S2), as given in the Judd-Ofelt theory,[45,46] and discussed in the references[43,47]. The sets of Ω_K (FED) values obtained, in units of 10^{-20} cm^2, are: Tb^{3+} $[\Omega_2 = 0.03;\ \Omega_4 = 0.19;\ \Omega_6 = 0.36]$ and Eu^{3+} $[\Omega_2 = 0.05;\ \Omega_4 = 0.36;\ \Omega_6 = 0.71]$. The W_{q-q}, W_{ex} and W_{md-md} mechanisms are independent of the Ω_K parameters.

In Equation 10, ρ_{f-f} is the overlap integral between 4*f* subshells of the donor and acceptor lanthanide ions. The values of ρ_{f-f} (Table S6) as a function of the Tb–Eu distance (R_L) were calculated using the parametric function $\rho_{f-f}(R_L) = exp(a + bR_L + cR_L^2)$, being $a = -0.032$,

$b = -0.261$, and $c = -0.34$.[48] The ρ_{f-f} decays very fast to zero with the increase of donor-acceptor distance R_L, as presented in Reference[31] for the case of Tb–Eu. This is the reason why the W_{ex} frequently can be neglected in the Ln–Ln energy transfer processes, where the donor-acceptor distances are, commonly, higher than 4 Å,[44] in contrast to the case of intramolecular energy transfer processes in lanthanide chelates.[44,47]

The nonradiative energy transfer involving magnetic dipole interactions in inorganic solids containing donor and acceptor ions has been treated in the early 1950s by Dexter[49] and Galanin[50], in the 1970s by Ermolaev[51,52], and in the 1990s by Tanner and collaborators.[53–55] The formulation of W_{md-md}, as presented in Equation 11, is found in the Reference [31].

The $\langle \psi J \| \, \| \psi^* J^* \rangle^2$ are doubly reduced matrix elements: the $\langle \psi J \| L + 2S \| \psi^* J^* \rangle^2$ were calculated (see Table S8) using the Ofelt's eigenfunctions in the intermediate coupling scheme,[56] and the $\langle \psi J \| U^{(K)} \| \psi^* J^* \rangle^2$ values were obtained from Reference[57] $\langle r^K \rangle$ are $4f$ radial integrals.[58] The shielding factors ($1 - \sigma_k$, with $k = 1$ and 2) were calculated according to:[59]

$$\left(1 - \sigma_k^{D,A}\right) = \rho (2\beta)^{k+1} \qquad (12)$$

where ρ and $\beta = (1 + \rho)^{-1}$ (values of ρ in Table S6) are quantities related to the Ln–Ligand chemical bond[47,60–62] and were estimated using the approach described in Reference [48]. $\mu_B \left(= \frac{e\hbar}{2m_e c}\right)$ in Equation 11 is the Bohr magneton in Gaussian-CGS units.

In all equations regarding the Ln-Ln energy transfer mechanisms, the spectral overlap factor (F) appears. This quantity is related to the energy mismatch conditions between the donor and acceptor states and the following expression for F has been used:[44]

$$F = \frac{\ln(2)}{\sqrt{\pi}} \frac{1}{\hbar^2 \gamma_{Tb} \gamma_{Eu}} \left\{ \left[\left(\frac{1}{\hbar\gamma_{Tb}} \right)^2 + \left(\frac{1}{\hbar\gamma_{Eu}} \right)^2 \right] \ln(2) \right\}^{-\frac{1}{2}} \times \exp\left[\frac{1}{4} \frac{\left(\frac{2\,\Delta E}{(\hbar\gamma_{Tb})^2} \ln 2 \right)^2}{\left[\left(\frac{1}{\hbar\gamma_{Eu}} \right)^2 + \left(\frac{1}{\hbar\gamma_{Tb}} \right)^2 \right] \ln 2} - \left(\frac{\Delta E}{\hbar\gamma_{Tb}} \right)^2 \ln(2) \right] \quad (13)$$

where $\hbar\gamma_{Tb}$ and $\hbar\gamma_{Eu}$ correspond to the bandwidths at half-height of the Tb^{3+} (donor) and Eu^{3+} (acceptor) transitions, respectively. ΔE is the energy difference between donor and acceptor transitions ($\Delta E = E_D - E_A$). Due to the strong shielding effect over the 4f electrons, the energy levels of the Ln^{3+} do not present significant shift with the changing of the environment, hence, the energy levels for LnF_3 can be employed in the calculus without any discrepancy (Table S7 for the comparison between transitions energies for Eu^{3+} and Tb^{3+} in LnF_3 and aqueous medium). In the present work, it will be considered the $\hbar\gamma_{Tb} = \hbar\gamma_{Eu} = 250\ cm^{-1}$, a value that is acceptable concerning the nature of 4*f* transitions.

The energy transfer pathways were chosen with the combination of four donor states (Tb^{3+}:$^5D_4 \rightarrow {}^7F_{3\text{-}6}$) and nine acceptor states (Eu^{3+}: $^7F_{0,1,2} \rightarrow {}^5D_{0,1,2}$), each pathway was labeled as shown **Table 4**. The selection rules on the *J* quantum numbers were also taken into account: $|J - J'| \leq K \leq J + J'$ for multipolar mechanisms (W_{d-d}, W_{d-q} and W_{q-q}); $\Delta J = 0, \pm 1$ for the magnetic dipole-magnetic dipole mechanism (W_{md-md}). The *J*-mixing effect will also be considered (see assumption 1 below), allowing the case of $J = J' = 0$. No defined selection rules on *J* appear for the exchange mechanism (W_{ex}).

For each pathway, the energy transfer rates were calculated by the sum over Equation 7 to 11 $\left(\omega = W_{d-d} + W_{d-q} + W_{q-q} + W_{ex} + W_{md-md}\right)$ and, when appropriate, the following points should be taken into account:[31]

1) In the case of the acceptor Eu^{3+} ion, the levels $^7F_0$, $^7F_1$, and $^7F_2$ are thermally dependent according to the Boltzmann distribution (0.65, 0.33, and 0.02 at 300 K, respectively[63]). In

the case of the pathway involving the $^7F_0 \rightarrow {}^5D_0$ transition, the *J*-mixing between the $^7F_0$ and $^7F_2$ levels (of the order of 5%) was considered.

2) When ΔE is negative (the donor state lies below the acceptor level), the energy transfer rates were multiplied by the barrier factor $\exp(\Delta E/k_B T)$, where k_B is Boltzmann's constant and T is the temperature. The case of pathway 9 (energy from $^5D_4 \rightarrow {}^7F_5$ to $^7F_1 \rightarrow {}^5D_1$, see Table 4) is an exception due to the resonance between the electronic Stark levels, as considered in References.[31,64]

3) W $(= \sum \omega)$ is the total rate for a specific donor-acceptor distance and it is multiplied by the occurrence $O_i(x)$ of exist a pair donor-acceptor at R_L, which decreases when x (Eu^{3+} content) increases.

The average donor-acceptor energy transfer rate $\langle W \rangle$ is given by:[31]

$$\langle W \rangle = \sum_i \langle W \rangle_i = (1 - x) \cdot x \cdot \left(\sum_i O_i(x) \cdot W_i \right) \qquad (14)$$

where W_i is the sum over all pathways for a specific R_L (assumption **3**). The Eu^{3+} ions concentration (x), as well as the Tb^{3+} ones $(1 - x)$, are considered explicitly. The coefficients O_i and c_i (from Reference [31]) have the same meaning. However, the latter case is obtained by a weighted-average of donor-acceptor while the coefficients in Equation 14 consists of a direct number of occurrences per Eu^{3+} of existing a pair Tb–Eu at the distance $R_L(i)$. Thus, the O_i can be obtained as:

$$O_i = \frac{\mathcal{N}(i)}{s \cdot x} \qquad (15)$$

where $\mathcal{N}$ is the average counting number of donor–acceptor pair present at distance $R_L(i)$, s is the number of host sites (Tb^{3+} ions) available for substitution by the Eu^{3+} one (x in fraction). The O_i also carries a dependence with the Eu^{3+} concentrations. For example, in an extremely

diluted system with a few Eu^{3+} ions, the condition $\lim_{x\to 0\%} O_i(x) = 1$ must be satisfied and, in the opposite situation $\lim_{x\to 100\%} O_i(x) = 0$. These limits are valid when the host and the donor ions are the same (Tb^{3+} ions), justifying the use of the pre-factor $(1-x)\cdot x$, otherwise, when $x \to 0\%$ (system without Eu^{3+} ions), the $\langle W \rangle$ do not converge to zero.

The coefficients $O_i(x)$ were obtained adapting a computer program[65] that simulates the doping process and extracts specifics Tb-Eu distances in a doped supercell (5×5×5, containing $s = 500$ Tb^{3+} sites) previously constructed from the crystallographic unit cell. The values of $O_i(x)$ are presented in Table S9.

Table 4 shows the rates of each pathway for the shortest distance R_L=4.35 Å, the most important for the overall energy transfer process. The energy transfer is dominated by far by the W_{q-q} mechanism (see pathway 9). This result agrees with the conclusions in References [66,67]. The exchange mechanism becomes more dominant (in the case of Tb–Eu energy transfer) when R_L is shorter than 4.12 Å, as in the case of $Ba_3Tb_{0.90}Eu_{0.10}(PO_4)_3$ eulytite.[31]

The W_1 (Table 4) denotes the sum over all individual pathways considering assumptions **1** and **2**. Pathway 9 (highlighted in bold) is the dominant one and does not include the barrier factor due to the resonance condition of the Stark levels. Beyond the first distance, the next two neighbor sites are located at 5.78 and 8.27 Å, although each of them has twice chance to form a Tb–Eu pair than the shortest one (Figure 3c), their contributions are expressively lower in one and three orders of magnitude (Table S9 and S10), respectively. It is worth to highlight that pathway 9 represents 89.36 (Table 4), 99.44 (Table S10), and 99.07% (Table S11) of the Tb-to-Eu total energy transfer. For this reason, from now it will be considered only the $(^5D_4 \rightarrow {}^7F_5) \rightarrow (^7F_1 \rightarrow {}^5D_1)$ energy transfer.

Applying the values of $\langle W \rangle$ of Equation (1) and using the $^5D_4$ lifetime in the absence of Eu^{3+} ion (τ_0=1.040×10^{-3} s, Table 1), one can estimate also the dependence of the $^5D_4$ lifetime τ with the Eu^{3+} content using:

$$\tau = \frac{1}{\left(\langle W \rangle + \frac{1}{\tau_0}\right)} \quad (16)$$

A good agreement between theoretical and experimental values of the energy transfer rates and $^5D_4$ lifetimes is depicted in **Figure 3d**.

When temperature increases, the population of $^7F_1$ also increases from $^7F_0$ obeying the Boltzmann's distribution that depends on the gap between the ground $^7F_0$ and first excited $^7F_1$ levels (~377 cm^{-1}, Supplementary Figure 25). Since the most relevant energy transfer pathway involves the $^7F_1$ level, the major energy transfer rate is blocked when $T \rightarrow 0$ K and starts to grow when the temperature rises.

Figure 3f shows both temperature and Eu^{3+} content effects upon the Tb-to-Eu energy transfer. The back energy transfer is not operative since the multiphonon relaxation from $^5D_1$ to $^5D_0$ is very high – in the order of 10^4 s^{-1} in $NaGdTiO_4:Eu^{3+}$ at 4.2 K[68] and more than 10^5 s^{-1} in $YVO_4:Eu^{3+}$ for temperature in the range of $100 < T < 600$ K[69] – digesting a fast depopulation of the $^5D_1$ level. The surface presented in Figure 3f was generated using 892 calculations of $\langle W \rangle$. The data were statistically treated by the weighted least squares method.[70]

Figure 4 presents the dependence of the performance parameters S_m and T_m with the $\langle W \rangle$ and with the Eu^{3+} content. The increase observed in the $\langle W \rangle$ with the Eu^{3+} content is also observed in the maximum relative thermal sensitivity (S_m) value suggesting a strong linear correlation between both quantities. Furthermore, for the temperature in which it occurs (T_m) we perceive the exact opposite trend (Figure 4).

From the qualitative point of view, the increase in the Tb-to-Eu energy transfer rate favors the depopulation of the $^5D_4$ level of Tb^{3+} with the temperature increase, and thus a higher slope in the $\Delta(T)$ curve is expected at its inflection point (in which the maximum sensitivity occurs), that is recorded at lower temperature values. In other words, our results point out that the higher the $\langle W \rangle$ value, the higher the S_m, favoring the performance of the luminescent thermometer.

The complete modelling of the thermal response of these mixed compounds that will certainly be useful for a detailed and quantitative optimization analysis is now underway and will be reported in future work.

6. Conclusion

The versatility of the tailored design of the MOFs has attracted attention for its potential application in luminescence thermometry in the last decade. Despite many works are studying the thermometric performance of a single sample or a series of samples, rare are the reports connecting the design and composition of the framework with the desired thermometric performance. In this work presented a series of $Tb_{1-x}Eu_x$ (x=0.030-0.150) MOF luminescent thermometers built upon isophtalic and acetic acids. The crystal structure is composed by Ln_2 SBUs connected by organic linkers to form a 3D network. We evidenced that this dimer topology promotes the presence of an efficient Tb^{3+}-to-Eu^{3+} energy transfer which varies from 77 to 93% when the Eu^{3+} content increases from 0.030 to 0.150. By increasing the Eu^{3+} content we observe a shift of 100 K towards low temperatures on T_m, connected to an increase in S_m from 0.19 to 0.44 %·K^{-1}. This variation on the S_m is partially explained by the increase of the nonradiative decay rate of the Tb^{3+} $^5D_4 \rightarrow {}^7F_5$ transition (relatively to the radiative one) with the increase of the Eu^{3+} doping. A detailed experimental and theoretical study on Tb-to-Eu energy transfer processes was very successful evidencing a notorious agreement between both. Using computer simulations we estimated the average (or effective) energy transfer rates using doping simulations and obtained the probability of occurrence of the donors-acceptor pairs, concluding that this energy transfer is dominated by the $^5D_4 \rightarrow {}^7F_5$ (Tb^{3+}) to $^7F_1 \rightarrow {}^5D_1$ (Eu^{3+}) pathway. Moreover, in line with the conclusions of recently published works,[31,66,67] we found out that the most relevant energy transfer mechanism is the quadrupole-quadrupole one, due to the shortest Tb-Eu distance that is 4.35 Å.

Comparing the energy barrier value extracted from the numerical simulations (260 cm^{-1} for the dominant pathway, Table 4) with those resulting from the Mott-Seitz analysis (~500-600 cm^{-1}, Table 2) we notice a factor of ~2 between them. Although the values are in the same order of magnitude, the discrepancy is supported by i) the assumption that the positions of the energy levels in the MOF were based on those reported by Carnall *et al*.[57] for the Ln^{3+}-doped lanthanum trifluoride; ii) the well-known fact that the Mott-Seitz model generally overestimates the energy barrier value;[71] and ii) the fitted ΔE value in Equation 4 is an effective energy gap involving the depopulation of the $^5D_4$ Tb^{3+} level by the $^5D_1$ Eu^{3+} one and the depopulation of the $^5D_0$ Eu^{3+} level by the triplet ligand level (explaining the temperature dependence of the $^5D_0 \rightarrow {}^7F_2$ transition).

We also perceive an increase in the Tb^{3+}-to-Eu^{3+} energy transfer rate with the temperature increase, what is strongly correlated to the enhancement of the maximum relative thermal sensitivity of the luminescent thermometer and with the concomitant decrease of the temperature at which the maximum thermal sensitivity is recorded.

The unique experimental and theoretical blended methodology presented here enabled us to rationally engineer the composition of the $Tb_{1-x}Eu_x$ mixed compound, looking forward to tunable thermal performance, a driving force paving the road for the future tailored-designing of molecular thermometers.

7. Experimental Section

Reagents and Chemicals: $Tb(NO_3)_3 \cdot 6H_2O$ (99.99%), $Eu(NO_3)_3 \cdot 6H_2O$ (99.99%), $Gd(NO_3)_3 \cdot 6H_2O$ (99.99%), and isophtalic acid (99%) were purchased from Alfa Aesar while acid acetic acid (99.8%) was purchased from Acros Organics. All chemicals were used without further purification.

Structural and Photophysical Characterization: Powder X-ray Diffraction spectra were monitored using a D8 Bruker diffractometer in the Bragg-Brentano geometry, equipped with a front germanium monochromator, a copper anode ($Cu_{K\text{-}L3}$ radiation λ=1.540598 Å) and a LynxEye PSD detector. The simulated pattern was obtained by the PowderCell 2.4 software from the cif file of the Eu-CP compound (CCDC 251041). Thermogravimetric analyses (TGA) were performed by flowing dry air with a heating and cooling rate of 5°C/min on a SETARAM TG-DSC 111 between 20 and 800°C. Fourier transform infrared (FT-IR) spectra were recorded in the 4000-400 cm^{-1} range on a Bruker Vertex FTIR spectrometer equipped with a computer control using the OPUS software. For ICP-AES analyses, samples were dissolved in a 10% HNO_3 solution and analyzed by ICP-AES. The calibration curve was established from the analysis of five standard solutions containing Eu and Tb in various contents to cover a range in accordance with targeted concentrations. The standard solutions were prepared with high purity monoelemental solutions in acidic solution. Photoluminescence spectra were recorded on a Jobin-Yvon Fluorolog 3 fluorometer equipped with a photomultiplier (excitation source: 450 W Xe arc lamp) using the front face acquisition mode. The emission spectra were corrected for detection and optical spectral response of the spectrofluorimeter and the excitation spectra were weighed for the spectral distribution of the lamp intensity using a photodiode reference detector. The temperature-dependent photoluminescence measurements were recorded on the same spectrometer controlling the temperature by a cryostat coupled with the Fluorolog cooled by liquid nitrogen. Lifetimes measurements were measured with the same equipment but the excitation was performed by a UV Xenon flash tube while the time-dependence of the emission was recorded with the photomultiplier.

Synthesis of $[Gd(CH_3COO)(1,3\text{-}bdc)(H_2O)_2]\cdot 0.5H_2O$ (Gd-CP): 1,3-H_2BDC (115 mg, 0.69 mmol) was dissolved in 5 mL of a NaOH solution (0.6 M) while $Gd(NO_3)_3{\cdot}6H_2O$ (258 mg,

0.69 mmol) was dissolved in 2 mL of deionized water containing glacial acetic acid (100 µL, 1.7 mmol). The two solutions were mixed and a white precipitate was formed. The pH of the mixture was adjusted at 5 by addition of a small amount of a NaOH solution (1.5 M). Then, the above mixture was placed in a sealed 21 ml Teflon lined stainless vessel, which was heated at 150°C for 72 h under autogenous pressure and cooled down to room temperature. The as-obtained white power was finally recovered by filtration and washed with EtOH. Yield: 0.218 g (37%). Anal. Calcd for $GdC_{10}H_{12}O_{8.5}$ (%): C, 28.23; H, 2.84. Found: C, 28.28; H, 2.57. IR (KBr pellet, cm^{-1}): 1605 (vs), 1547 (vs), 1479 (s), 1466 (s), 1447 (s), 1408 (vs), 1385 (s), 1369 (s), 1317 (w), 1279 (w), 1165 (w), 1103 (w), 1082 (w), 1024 (w), 961 (w), 831 (m), 743 (s), 721 (m), 687 (m), 613 (m), 575 (m), 525 (m).

Synthesis of $[Eu(CH_3COO)(1,3\text{-}bdc)(H_2O)_2]\cdot 0.5H_2O$ *(Eu-CP):* 1,3-H_2BDC (115 mg, 0.69 mmol) was dissolved in 5 mL of a NaOH solution (0.6 M) while $Eu(NO_3)_3\cdot 6H_2O$ (296 mg, 0.69 mmol) was dissolved in 2 mL of deionized water containing glacial acetic acid (100 µL, 1.7 mmol). The two solutions were mixed and a white precipitate was formed. The pH of the mixture was adjusted at 5 by addition of a small amount of a NaOH solution (1.5 M). Then, the above mixture was placed in a sealed 21 ml Teflon lined stainless vessel, which was heated at 150°C for 72 h under autogenous pressure and cooled down to room temperature. The as-obtained white power was finally recovered by filtration and washed with EtOH. Yield: 0.238 g (41%). Anal. Calcd for $EuC_{10}H_{12}O_{8.5}$ (%): C, 28.60; H, 2.90. Found: C, 28.54; H, 2.54. IR (KBr pellet, cm^{-1}): 1605 (vs), 1549 (vs), 1479 (s), 1466 (s), 1447 (s), 1410 (vs), 1385 (s), 1371 (s), 1317 (w), 1279 (w), 1165 (w), 1103 (w), 1082 (w), 1024 (w), 959 (w), 829 (m), 744 (s), 721 (m), 685 (m), 613 (m), 573 (m), 523 (m).

Synthesis of [Tb(CH$_3$COO)(1,3-bdc)(H$_2$O)$_2$]·0.5H$_2$O (Tb-CP): 1,3-H$_2$BDC (115 mg, 0.69 mmol) was dissolved in 5 mL of a NaOH solution (0.6 M) while Tb(NO$_3$)$_3$·6H$_2$O (290 mg, 0.69 mmol) was dissolved in 2 mL of deionized water containing glacial acetic acid (100 µL, 1.7 mmol). The two solutions were mixed and a white precipitate was formed. The pH of the mixture was adjusted at 5 by addition of a small amount of a NaOH solution (1.5 M). Then, the above mixture was placed in a sealed 21 ml Teflon lined stainless vessel, which was heated at 150°C for 72 h under autogenous pressure and cooled down to room temperature. The as-obtained white power was finally recovered by filtration and washed with EtOH. Yield: 0.242 g (41%). Anal. Calcd for TbC$_{10}$H$_{12}$O$_{8.5}$ (%): C, 28.10; H, 2.80. Found: C, 28.04; H, 2.56. IR (KBr pellet, cm^{-1}): 1605 (vs), 1551 (vs), 1479 (s), 1468 (s), 1448 (s), 1410 (vs), 1385 (s), 1371 (s), 1317 (w), 1279 (w), 1167 (w), 1103 (w), 1082 (w), 1026 (w), 962 (w), 831 (m), 744 (s), 719 (m), 689 (m), 613 (m), 575 (m), 525 (m).

Synthesis of [Tb$_{1-x}$Eu$_x$(CH$_3$COO)(1,3-bdc)(H$_2$O)$_2$]·0.5H$_2$O (Tb$_{1-x}$Eu$_x$): 1,3-H$_2$BDC (115 mg, 0.69 mmol) was dissolved in 5 mL of a NaOH solution (0.6 M) while Tb(NO$_3$)$_3$·6H$_2$O and Eu(NO$_3$)$_3$·6H$_2$O in the appropriate ratio was dissolved in 2 mL of deionized water containing glacial acetic acid (100 µL, 1.7 mmol). The two solutions were mixed and a white precipitate was formed. The pH of the mixture was adjusted at 5 by addition of a small amount of a NaOH solution (1.5 M). Then, the above mixture was placed in a sealed 21 ml Teflon lined stainless vessel, which was heated at 150°C for 72 h under autogenous pressure and cooled down to room temperature. The as-obtained white power was finally recovered by filtration and washed with EtOH. For the whole series, the chemical yields were around 40%. The targeted compositions for Tb$_{1-x}$Eu$_x$ was x = 0.030, 0.050, 0.075, 0.100, 0.125 and 0.150. The Tb/Eu molar ratio was checked by IPC-AES, the experimental compositions are reported in Table S1.

Supporting Information

Supporting Information is available from the Wiley Online Library or from the author.

Acknowledgements

This work was developed within the scope of the project CICECO – Aveiro Institute of Materials, UIDB/50011/2020, financed by Portuguese funds through the FCT/MEC and when appropriate co-financed by FEDER under the PT2020 Partnership Agreement. Financial support from NanoHeatControl project (POCI-01-0145-FEDER-031469), funded by FEDER, through POCI and by Portuguese funds (OE), through FCT/MCTES is also acknowledged. V.T. and A.N.C.N. thanks la Fondation de la Maison de la Chimie and the SusPhotoSolutions project, CENTRO-01-0145-FEDER-000005 Portugal, respectively, for their postdoctoral fellowships.

Received: ((will be filled in by the editorial staff))
Revised: ((will be filled in by the editorial staff))
Published online: ((will be filled in by the editorial staff))

References

[1] H.-C. Zhou, S. Kitagawa, *Chem. Soc. Rev.* **2014**, *43*, 5415.

[2] S. T. Madrahimov, J. R. Gallagher, G. Zhang, Z. Meinhart, S. J. Garibay, M. Delferro, J. T. Miller, O. K. Farha, J. T. Hupp, S. T. Nguyen, *ACS Catal.* **2015**, *5*, 6713.

[3] T. Sawano, N. C. Thacker, Z. Lin, A. R. McIsaac, W. Lin, *J. Am. Chem. Soc.* **2015**, *137*, 12241.

[4] Y.-B. Zhang, H. Furukawa, N. Ko, W. Nie, H. J. Park, S. Okajima, K. E. Cordova, H. Deng, J. Kim, O. M. Yaghi, *J. Am. Chem. Soc.* **2015**, *137*, 2641.

[5] H. L. Nguyen, N. Hanikel, S. J. Lyle, C. Zhu, D. M. Proserpio, O. M. Yaghi, *J. Am. Chem. Soc.* **2020**, *142*, 2218.

[6] K. Binnemans, *Chem. Rev.* **2009**, *109*, 4283.

[7] J. Rocha, L. D. Carlos, F. A. A. Paz, D. Ananias, *Chem. Soc. Rev.* **2011**, *40*, 926.

[8] Y. Cui, B. Li, H. He, W. Zhou, B. Chen, G. Qian, *Acc. Chem. Res.* **2016**, *49*, 483.

[9] W. P. Lustig, S. Mukherjee, N. D. Rudd, A. V. Desai, J. Li, S. K. Ghosh, *Chem. Soc. Rev.* **2017**, *46*, 3242.

[10] C. D. S. Brites, P. P. Lima, N. J. O. Silva, A. Millán, V. S. Amaral, F. Palacio, L. D. Carlos, *New J. Chem.* **2011**, *35*, 1177.

[11] D. Jaque, F. Vetrone, *Nanoscale* **2012**, *4*, 4301.

[12] X. D. Wang, O. S. Wolfbeis, R. J. Meier, *Chem. Soc. Rev.* **2013**, *42*, 7834.

[13] Y. Cui, F. Zhu, B. Chen, G. Qian, *Chem. Commun.* **2015**, *51*, 7420.

[14] C. D. S. Brites, A. Millán, L. D. Carlos, in *Handb. Phys. Chem. Rare Earths* (Eds.: J.-C.G. Bünzli, V.K. Pecharsky), Elsevier, **2016**, pp. 339–427.

[15] J. Rocha, C. D. S. Brites, L. D. Carlos, *Chem. - A Eur. J.* **2016**, *22*, 14782.

[16] C. D. S. Brites, S. Balabhadra, L. D. Carlos, *Adv. Opt. Mater.* **2019**, *7*, 1.

[17] G. E. Gomez, R. Marin, A. N. Carneiro Neto, A. M. P. Botas, J. Ovens, A. A. Kitos, M. C. Bernini, L. D. Carlos, G. J. A. A. Soler-Illia, M. Murugesu, *Chem. Mater.* **2020**, *32*, 7458.

[18] C. D. S. Brites, P. P. Lima, N. J. O. Silva, A. Millan, V. S. Amaral, F. Palacio, L. D. Carlos, *Nanoscale* **2012**, *4*, 4799.

[19] O. A. Savchuk, J. J. Carvajal, J. Massons, C. Cascales, M. Aguilo, F. Diaz, *Sensors Actuators, A Phys.* **2016**, *250*, 87.

[20] M. Quintanilla, L. M. Liz-marzán, *Nano Today* **2018**, *19*, 126.

[21] Y. Cui, H. Xu, Y. Yue, Z. Guo, J. Yu, Z. Chen, J. Gao, Y. Yang, G. Qian, B. Chen, *J. Am. Chem. Soc.* **2012**, *134*, 3979.

[22] X. Rao, T. Song, J. Gao, Y. Cui, Y. Yang, C. Wu, B. Chen, G. Qian, *J. Am. Chem. Soc.*

2013, *135*, 15559.

[23] I. N'Dala-Louika, D. Ananias, C. Latouche, R. Dessapt, L. D. Carlos, H. Serier-Brault, *J. Mater. Chem. C* **2017**, *5*, 10933.

[24] C.-G. Zheng, J. Zhang, Z.-F. Chen, Z.-J. Guo, R.-G. Xiong, X.-Z. You, *J. Coord. Chem.* **2002**, *55*, 835.

[25] X.-J. Zheng, T.-T. Zheng, L.-P. Jin, *J. Mol. Struct.* **2005**, *740*, 31.

[26] Y. Jin, F. Luo, Y. Che, J. M. Zheng, *Inorg. Chem. Commun.* **2008**, *11*, 711.

[27] L. Yang, S. Song, C. Shao, W. Zhang, H. Zhang, Z. Bu, T. Ren, *Synth. Met.* **2011**, *161*, 1500.

[28] C. Song, X. Li, W. Liu, Z. Cao, Y. Ren, Q. Zhou, L. Zhang, *Synth. React. Inorganic, Met. Nano-Metal Chem.* **2016**, *46*, 1174.

[29] M. Latva, H. Takalo, V.-M. Mukkala, C. Matachescu, J. C. Rodríguez-Ubis, J. Kankare, *J. Lumin.* **1997**, *75*, 149.

[30] L. J. Charbonniere, N. Hildebrandt, R. F. Ziessel, H.-G. Loehmannsroeben, *J. Am. Chem. Soc.* **2006**, *128*, 12800.

[31] A. N. Carneiro Neto, R. T. Moura, A. Shyichuk, V. Paterlini, F. Piccinelli, M. Bettinelli, O. L. Malta, *J. Phys. Chem. C* **2020**, *10*, 10105.

[32] H.-Y. D. Ke, E. R. Birnbaum, *J. Lumin.* **1995**, *63*, 9.

[33] R. Reisfeld, **1973**, pp. 53–98.

[34] Mott N. F., *Proc. R. Soc. London. Ser. A. Math. Phys. Sci.* **1938**, *167*, 384.

[35] F. Seitz, *Trans. Faraday Soc.* **1939**, *35*, 74.

[36] A. Cadiau, C. D. S. Brites, P. M. F. J. Costa, R. A. S. Ferreira, J. Rocha, L. D. Carlos, *ACS Nano* **2013**, *7*, 7213.

[37] Y. Zhou, B. Yan, F. Lei, *Chem. Commun.* **2014**, *50*, 15235.

[38] D. Zhao, X. Rao, J. Yu, Y. Cui, Y. Yang, G. Qian, *Inorg. Chem.* **2015**, *54*, 11193.

[39] Y. Zhou, B. Yan, D. Z. Tan, J. J. Zhou, Q. B. Guo, W. Jiang, C. Xu, X. F. Liu, J. R. Qiu, R. S. Liu, X. Y. Chen, *Nanoscale* **2015**, *7*, 4063.

[40] T. Chuasaard, A. Ngamjarurojana, S. Surinwong, T. Konno, S. Bureekaew, A. Rujiwatra, *Inorg. Chem.* **2018**, *57*, 2620.

[41] P. Farger, C. Leuvrey, M. Gallart, P. Gilliot, G. Rogez, J. Rocha, D. Ananias, P. Rabu, E. Delahaye, *Beilstein J. Nanotechnol.* **2018**, *9*, 2775.

[42] X. Zhou, H. Wang, S. Jiang, G. Xiang, X. Tang, X. Luo, L. Li, X. Zhou, *Inorg. Chem.* **2019**, *58*, 3780.

[43] T. Kushida, *J. Phys. Soc. Japan* **1973**, *34*, 1318.

[44] O. L. Malta, *J. Non. Cryst. Solids* **2008**, *354*, 4770.

[45] B. R. Judd, *Phys. Rev.* **1962**, *127*, 750.

[46] G. S. Ofelt, *J. Chem. Phys.* **1962**, *37*, 511.

[47] A. N. Carneiro Neto, E. E. S. Teotonio, G. F. de Sá, H. F. Brito, J. Legendziewicz, L. D. Carlos, M. C. F. C. Felinto, P. Gawryszewska, R. T. Moura Jr., R. L. Longo, W. M. Faustino, O. L. Malta, in *Handb. Phys. Chem. Rare Earths, Vol. 56*, Elsevier, **2019**, pp. 55–162.

[48] A. N. Carneiro Neto, R. T. Moura Jr., *Chem. Phys. Lett.* **2020**, *757*, 137884.

[49] D. L. Dexter, *J. Chem. Phys.* **1953**, *21*, 836.

[50] I. M. D. Galanin, I. M. Frank, *Zh. Eksperim. i Teor. Fiz* **1951**, *21*, 114.

[51] V. L. Ermolaev, E. B. Sveshnikova, *J. Lumin.* **1979**, *20*, 387.

[52] E. B. Sveshnikova, V. L. Ermolaev, *Opt. Spectrosc.* **2011**, *111*, 34.

[53] P. A. Tanner, M. Chua, M. F. Reid, *J. Alloys Compd.* **1995**, *225*, 20.

[54] M. Chua, P. A. Tanner, M. F. Reid, *J. Lumin.* **1994**, *58*, 356.

[55] M. Chua, P. A. Tanner, M. F. Reid, *Solid State Commun.* **1994**, *90*, 581.

[56] G. S. Ofelt, *J. Chem. Phys.* **1963**, *38*, 2171.

[57] W. T. Carnall, H. Crosswhite, H. M. Crosswhite, *Energy Level Structure and Transition Probabilities in the Spectra of the Trivalent Lanthanides in LaF_3*, Argonne, IL (United States), IL (United States), **1978**.

[58] S. Edvardsson, M. Klintenberg, *J. Alloys Compd.* **1998**, *275–277*, 230.

[59] O. L. Malta, H. F. Brito, J. F. S. Menezes, F. R. G. e Silva, S. Alves, F. S. Farias, A. V. M. de Andrade, *J. Lumin.* **1997**, *75*, 255.

[60] O. L. Malta, *Chem. Phys. Lett.* **1982**, *87*, 27.

[61] O. L. Malta, H. J. Batista, L. D. Carlos, *Chem. Phys.* **2002**, *282*, 21.

[62] R. T. Moura, A. N. Carneiro Neto, R. L. Longo, O. L. Malta, *J. Lumin.* **2016**, *170*, 420.

[63] A. S. Souza, L. A. O. Nunes, I. G. N. Silva, F. A. M. Oliveira, L. L. Da Luz, H. F. Brito, M. C. F. C. Felinto, R. A. S. Ferreira, S. A. Júnior, L. D. Carlos, O. L. Malta, *Nanoscale* **2016**, *8*, 5327.

[64] M. T. Berry, P. S. May, Q. Hu, *J. Lumin.* **1997**, *71*, 269.

[65] F. J. Caixeta, A. R. N. Bastos, A. M. P. Botas, L. S. Rosa, V. S. Souza, F. H. Borges, A. N. C. Neto, A. Ferrier, P. Goldner, L. D. Carlos, R. R. Gonçalves, R. A. S. Ferreira, *J. Phys. Chem. C* **2020**, *124*, 19892.

[66] A. Shyichuk, S. S. Câmara, I. T. Weber, A. N. Carneiro Neto, L. A. O. Nunes, S. Lis, R. L. Longo, O. L. Malta, *J. Lumin.* **2016**, *170*, 560.

[67] A. N. Carneiro Neto, R. T. Moura, O. L. Malta, *J. Lumin.* **2019**, *210*, 342.

[68] P. A. M. Berdowski, G. Blasse, *Chem. Phys. Lett.* **1984**, *107*, 351.

[69] E. D. Reed, H. W. Moos, *Phys. Rev. B* **1973**, *8*, 988.

[70] Wasserman L., *All of Nonparametric Statistics*, Springer New York, **2006**.

[71] G. Blasse, *Nonradiative Processes in Luminescent Materials: A Materials Scientists View*, New York: NATO Advanced Study Institute Series, Plenum Press, New York, **1990**.

Figures

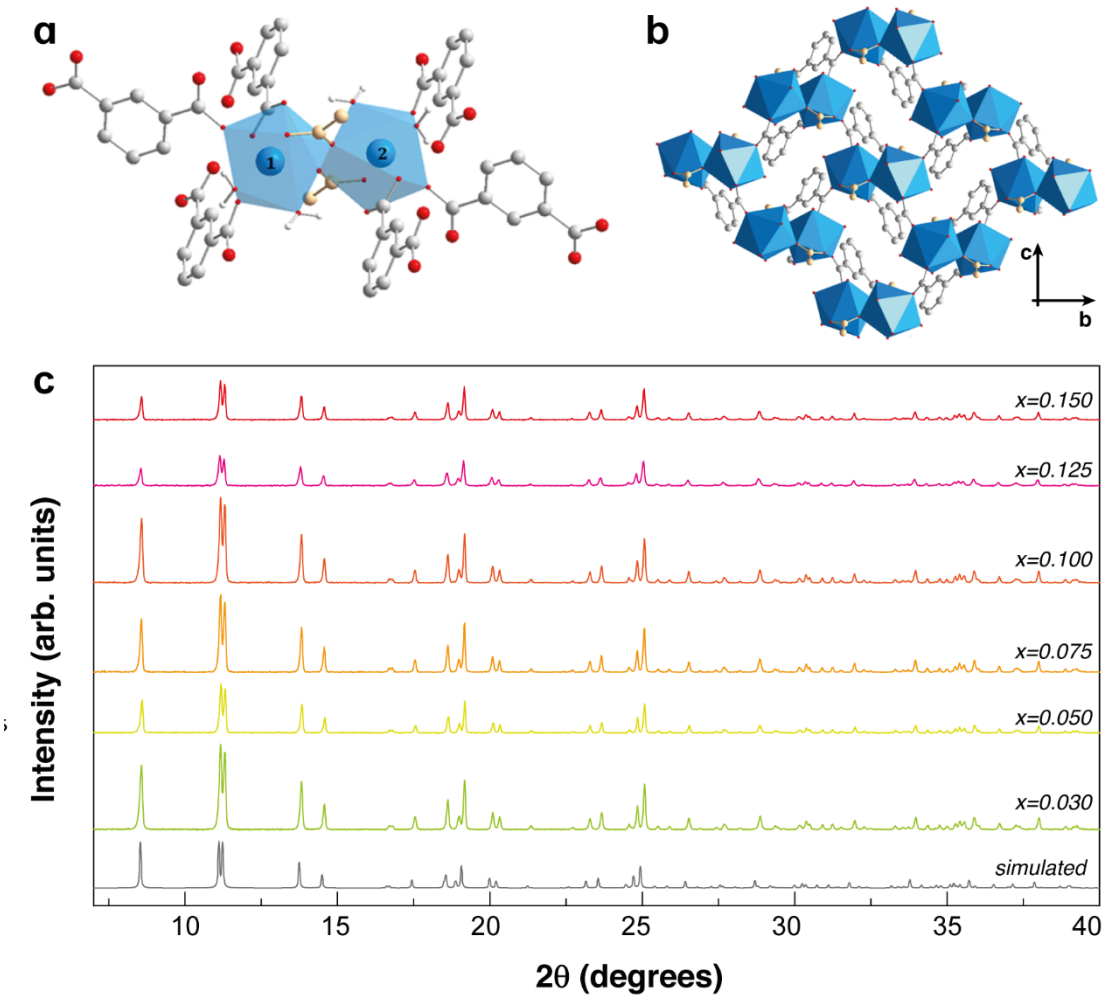

Figure 1. (a) Representation of Ln_2SBU formed by two symmetric [LnO_9] polyhedron linked by an edge formed by two acetate ligand (color code: blue for Ln^{3+}, grey for carbon, red for oxygen, yellow for the acetate ligands and white for water hydrogens). H atoms of carboxylate ligands are omitted for more clarity. **(b)** Representation of the crystal structure along the *a*-axis. **(c)** X-ray diffraction patterns of $Tb_{1-x}Eu_x$ compounds. The bottom line corresponds to the simulated profile of the Eu-CP.

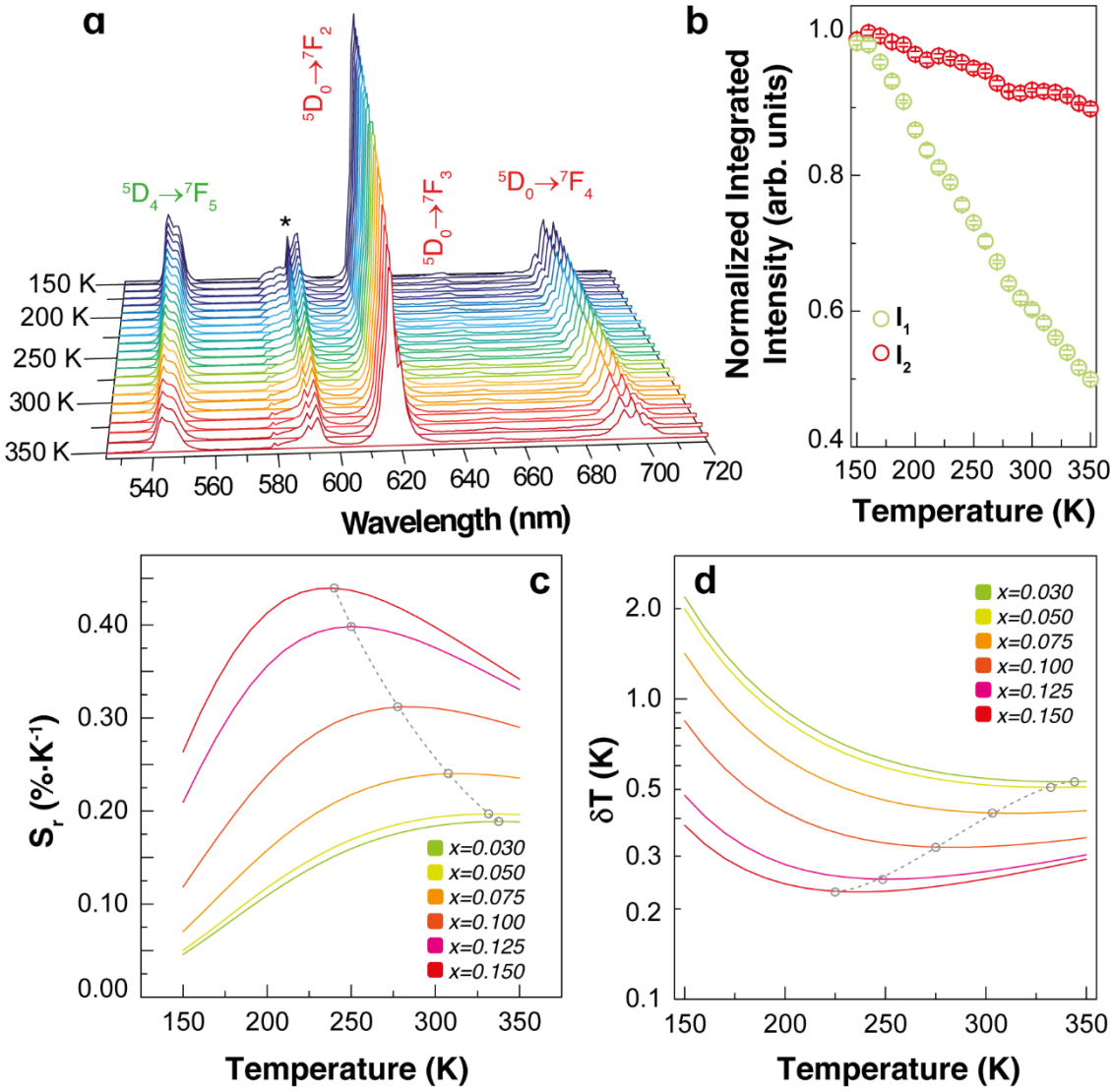

Figure 2 (a) Temperature-dependent emission spectra in the 150-350 K range of $Tb_{0.950}Eu_{0.050}$ upon 289 nm excitation. **(b)** Corresponding dependence of the normalized integrated areas of I_1 (Tb^{3+}, $^5D_4 \rightarrow {}^7F_5$) and I_2 (Eu^{3+}, $^5D_0 \rightarrow {}^7F_2$). **(c)** Relative thermal sensitivity for the mixed compounds and **(d)** temperature uncertainty in the 150-350 K range. The dots mark the S_m values and the minimum δT values, respectively in panels c and d, and the interrupted lines are guides for the eyes.

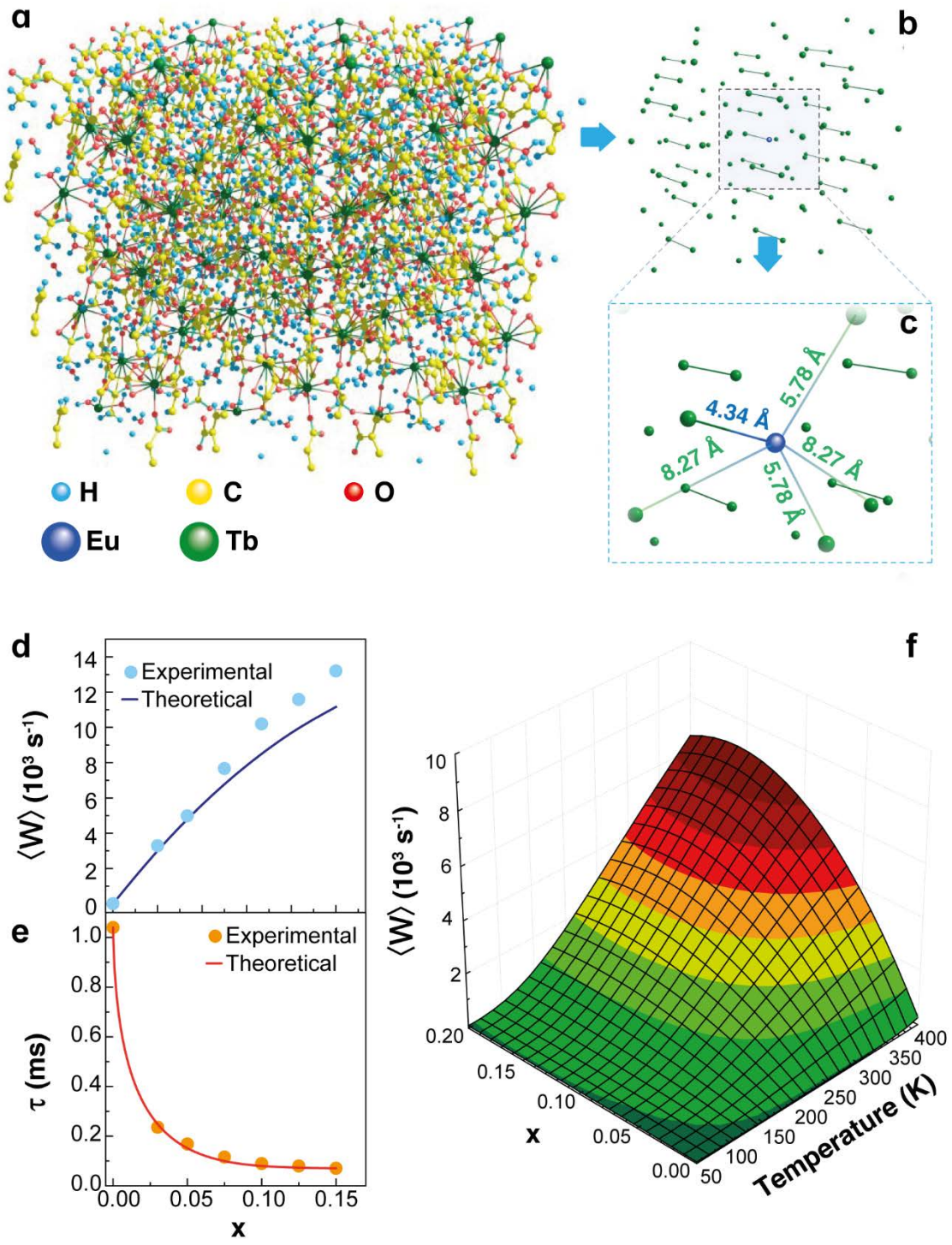

Figure 3. (a) Representation of a 3×3×3 cell of the doped Tb-CP. Scheme of **(b)** the isolation of the neighbors' ions and **(c)** the extraction of the donor–acceptors distances. **(d)** Tb^{3+}-to-Eu^{3+} nonradiative energy transfer rates obtained using Equation 1 (points) and Equation 14 (line). **(e)** $^5D_4$ lifetime values (Equation 16 and Table 1) as a function of the Eu^{3+} content (x). **(f)** Tb^{3+}-to-Eu^{3+} energy transfer rate $\langle W \rangle$ as a function of the Eu^{3+} content and of the temperature for $Tb_{1-x}Eu_x$ compounds.

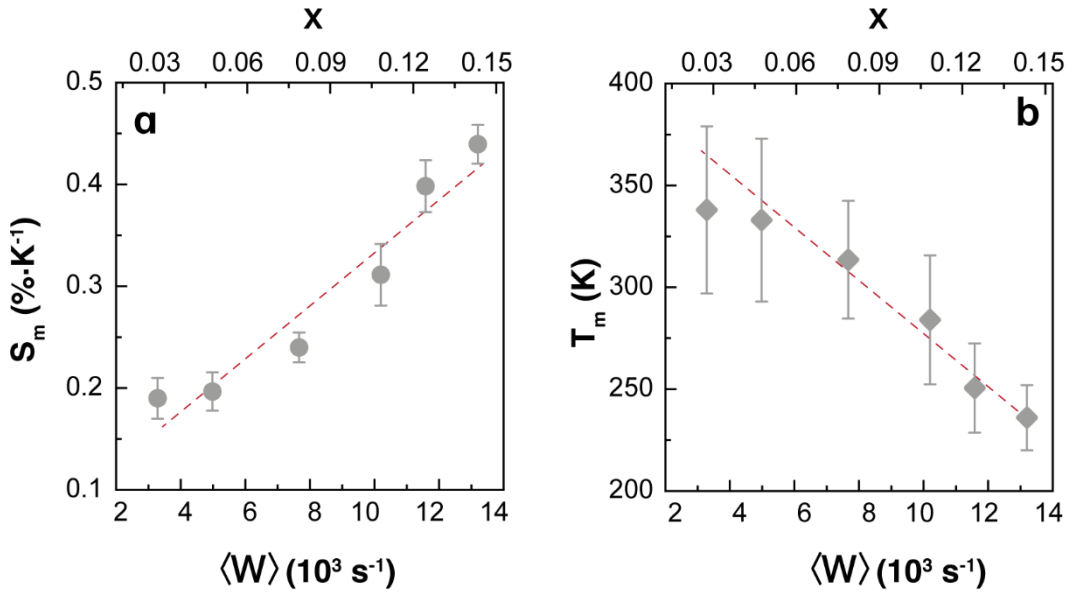

Figure 4. (a) Maximum relative thermal sensitivity and **(b)** temperature value at which it occurs against the calculated Tb^{3+}-to-Eu^{3+} energy transfer rate $\langle \boldsymbol{W} \rangle$ for the $Tb_{1-x}Eu_x$ compounds. The lines are guides for the eyes.

Tables

Table 1. The $^5D_4$ (monitoring at 545 nm) and $^5D_0$ level (monitoring at 615 nm) lifetimes and Tb^{3+}-to-Eu^{3+} energy transfer efficiency (η_{ET}) in the single-doped and mixed $Tb_{1-x}Eu_x$ samples at 300 K. The excitation wavelength is 289 nm.

Sample	*x*	$^5D_4$ (10^{-3} s)	$^5D_0$ (10^{-3} s)	η_{ET} (%)
Eu-CP	-	-	0.39 ± 0.05	-
Tb-CP	-	1.19 ± 0.08	-	-
$Tb_{1-x}Eu_x$	0.030	0.28 ± 0.04	0.49 ± 0.05	76 ± 4
	0.050	0.17 ± 0.04	0.45 ± 0.05	84 ± 3
	0.075	0.12 ± 0.04	0.42 ± 0.04	89 ± 3
	0.100	0.09 ± 0.04	0.42 ± 0.04	91 ± 3
	0.125	0.08 ± 0.04	0.40 ± 0.03	92 ± 3
	0.150	0.08± 0.04	0.48 ± 0.05	92 ± 3

Table 2. Fitting parameters of Equation 4 to the experimental $\Delta(T)$ for the $Tb_{1-x}Eu_x$ compounds.

x	Δ_0	α	ΔE (cm^{-1})	r^2
0.030	0.67±0.01	4.46±0.53	620±26	0.9999
0.050	0.67±0.01	4.65±0.50	614±31	0.9999
0.075	0.19±0.01	5.90±0.40	600±22	0.9999
0.100	0.27±0.01	7.94±0.93	570±30	0.9998
0.125	0.14±0.01	10.00±0.91	522±10	0.9999
0.150	0.41±0.01	10.87±0.40	500±18	0.9999

Table 3. Thermometric performance of the mixed compounds reported here compared with illustrative examples of the literature.

Material	*Eu content*	S_m (%·K^{-1})	δT_m (K)	T_m (K)	*Reference*
$Tb_{1-x}Eu_x$	x=0.030	0.19±0.02	0.53	338±41	This work
	x=0.050	0.20±0.02	0.51	333±40	
	x=0.075	0.24±0.01	0.42	314±29	
	x=0.100	0.31±0.03	0.32	284±32	
	x=0.125	0.40±0.02	0.25	251±22	
	x=0.150	0.44±0.02	0.23	236±16	
$Tb_{0.99}Eu_{0.01}(bdc)_{1.5}(H_2O)_2$	x=0.01	0.37		318	[36]
$Tb_{0.80}Eu_{0.20}$BPA	x=0.20	1.19		313	[38]
Eu^{3+}@UiO-bpydc	x=0.001	2.19*		293	[37]
$Tb_{0.995}Eu_{0.005}$ @In(OH)-bpydc	x=0.0005	4.47*		333	[37]
$Tb_{1-x}Eu_x(ad)_{0.5}$ $(phth)(H_2O)_2$	x=0.001	0.42		303	[40]
	x=0.003	0.59		303	
	x=0.005	1.21		303	
$Tb_{0.97}Eu_{0.03}(L)(ox)(H_2O)$	x=0.03	1.38		340	[41]
$Tb_{1.95}Eu_{0.05}$-PDC	x=0.05	0.64		318	[42]

bdc = 1,4-benzenedicarboxylic acid, BPA = biphenyl-3,5-dicarboxylic acid, bpydc = 2,2'-bipyridine-5,5'-dicarboxylic acid, ad = adipic acid, phth = phthalic acid, L =1,3-bis(carboxymethyl-)-imidazolium, ox = oxalic acid, PDC = pyridine-3,5-dicarboxylic acid.

* values recalculated in reference[41]

Table 4. Pairwise nonradiative energy transfer rates (s^{-1}) from Tb^{3+} to Eu^{3+} at the shortest distance (R_L=4.35 Å).

Pathway Label	Tb^{3+}	Eu^{3+}	ΔE	W_{d-d}	W_{d-q}	W_{q-q}	W_{ex}	W_{md-md}	ω
1	$^5D_4 \rightarrow {}^7F_6$	$^7F_1 \rightarrow {}^5D_0$	3521	0.0	0.0	0.0	4.5×10^{-26}	0.0	1.5×10^{-26}
2	$^5D_4 \rightarrow {}^7F_6$	$^7F_0 \rightarrow {}^5D_0$	3149	6.1×10^{-27}	3.3×10^{-23}	7.6×10^{-20}	4.2×10^{-20}	0.0	1.9×10^{-22}
3	$^5D_4 \rightarrow {}^7F_6$	$^7F_1 \rightarrow {}^5D_1$	1787	2.5×10^{-11}	1.3×10^{-7}	3.1×10^{-4}	6.5×10^{-4}	0.0	3.2×10^{-4}
4	$^5D_4 \rightarrow {}^7F_5$	$^7F_1 \rightarrow {}^5D_0$	1473	0.0	0.0	0.0	1.9×10^{-1}	1.2×10^{-4}	6.3×10^{-2}
5	$^5D_4 \rightarrow {}^7F_6$	$^7F_0 \rightarrow {}^5D_1$	1415	0.0	0.0	0.0	4.8×10^{-1}	0.0	3.1×10^{-1}
6	$^5D_4 \rightarrow {}^7F_5$	$^7F_0 \rightarrow {}^5D_0$	1101	1.3×10^{-5}	9.3×10^{-2}	1.1×10^{3}	3.9×10^{1}	0.0	1.8
7	$^5D_4 \rightarrow {}^7F_4$	$^7F_1 \rightarrow {}^5D_0$	206	0.0	0.0	0.0	2.5×10^{4}	6.2	8.4×10^{3}
8	$^5D_4 \rightarrow {}^7F_4$	$^7F_0 \rightarrow {}^5D_0$	−166	5.7×10^{-3}	2.9×10^{1}	1.1×10^{4}	2.7×10^{4}	0.0	2.8×10^{1}
9	**$^5D_4 \rightarrow {}^7F_5$**	**$^7F_1 \rightarrow {}^5D_1$**	**−260**	**2.7×10^{-3}**	**2.0×10^{1}**	**2.4×10^{5}**	**3.2×10^{4}**	**1.6×10^{-1}**	**8.8×10^{4}**
10	$^5D_4 \rightarrow {}^7F_5$	$^7F_0 \rightarrow {}^5D_1$	−633	0.0	0.0	0.0	3.5×10^{3}	1.6	1.1×10^{2}
11	$^5D_4 \rightarrow {}^7F_6$	$^7F_1 \rightarrow {}^5D_2$	−669	0.0	0.0	0.0	2.7×10^{3}	0.0	3.6×10^{1}
12	$^5D_4 \rightarrow {}^7F_3$	$^7F_1 \rightarrow {}^5D_0$	−773	0.0	0.0	0.0	1.2×10^{3}	3.1	9.5
13	$^5D_4 \rightarrow {}^7F_6$	$^7F_0 \rightarrow {}^5D_2$	−1041	0.0	0.0	0.0	7.9×10^{1}	0.0	9.6×10^{-1}
14	$^5D_4 \rightarrow {}^7F_3$	$^7F_0 \rightarrow {}^5D_0$	−1145	1.9×10^{-6}	1.2×10^{-2}	9.8×10^{1}	2.2×10^{1}	0.0	7.9×10^{-4}
15	$^5D_4 \rightarrow {}^7F_4$	$^7F_1 \rightarrow {}^5D_1$	−1528	4.1×10^{-9}	2.1×10^{-5}	7.9×10^{-3}	7.6×10^{-2}	1.5×10^{-7}	1.8×10^{-5}
16	$^5D_4 \rightarrow {}^7F_4$	$^7F_0 \rightarrow {}^5D_1$	−1900	0.0	0.0	0.0	6.5×10^{-5}	1.1×10^{-8}	4.6×10^{-9}
17	$^5D_4 \rightarrow {}^7F_3$	$^7F_1 \rightarrow {}^5D_1$	−2507	5.2×10^{-19}	3.3×10^{-15}	2.7×10^{-11}	2.3×10^{-11}	5.1×10^{-16}	9.9×10^{-17}
18	$^5D_4 \rightarrow {}^7F_5$	$^7F_1 \rightarrow {}^5D_2$	−2717	0.0	0.0	0.0	5.3×10^{-14}	1.3×10^{-18}	3.9×10^{-20}
19	$^5D_4 \rightarrow {}^7F_3$	$^7F_0 \rightarrow {}^5D_1$	−2879	0.0	0.0	0.0	3.5×10^{-16}	6.6×10^{-19}	2.3×10^{-22}
20	$^5D_4 \rightarrow {}^7F_5$	$^7F_0 \rightarrow {}^5D_2$	−3089	0.0	0.0	0.0	3.4×10^{-19}	0.0	2.3×10^{-24}
21	$^5D_4 \rightarrow {}^7F_4$	$^7F_1 \rightarrow {}^5D_2$	−3984	0.0	0.0	0.0	1.9×10^{-34}	1.8×10^{-39}	3.2×10^{-43}
22	$^5D_4 \rightarrow {}^7F_4$	$^7F_0 \rightarrow {}^5D_2$	−4356	0.0	0.0	0.0	6.5×10^{-42}	0.0	4.9×10^{-51}
23	$^5D_4 \rightarrow {}^7F_3$	$^7F_1 \rightarrow {}^5D_2$	−4963	0.0	0.0	0.0	1.5×10^{-55}	1.6×10^{-59}	2.3×10^{-66}
24	$^5D_4 \rightarrow {}^7F_3$	$^7F_0 \rightarrow {}^5D_2$	−5335	0.0	0.0	0.0	9.2×10^{-65}	0.0	2.4×10^{-75}
25	$^5D_4 \rightarrow {}^7F_6$	$^7F_2 \rightarrow {}^5D_0$	4177	8.9×10^{-46}	4.8×10^{-42}	1.1×10^{-38}	3.1×10^{-38}	0.0	8.4×10^{-40}
26	$^5D_4 \rightarrow {}^7F_6$	$^7F_2 \rightarrow {}^5D_1$	2443	0.0	0.0	0.0	1.4×10^{-10}	0.0	2.7×10^{-12}
27	$^5D_4 \rightarrow {}^7F_6$	$^7F_2 \rightarrow {}^5D_2$	-13	3.8×10^{-3}	3.9	6.5×10^{3}	3.2×10^{4}	0.0	7.2×10^{2}

28	$^5D_4 \rightarrow {}^7F_5$	$^7F_2 \rightarrow {}^5D_0$	2129	2.6×10^{-14}	1.9×10^{-10}	2.2×10^{-6}	3.9×10^{-7}	0.0	5.2×10^{-8}
29	$^5D_4 \rightarrow {}^7F_5$	$^7F_2 \rightarrow {}^5D_1$	395	0.0	0.0	0.0	1.3×10^{4}	1.7×10^{2}	2.7×10^{2}
30	$^5D_4 \rightarrow {}^7F_5$	$^7F_2 \rightarrow {}^5D_2$	-2061	5.2×10^{-13}	1.5×10^{-9}	6.0×10^{-6}	1.9×10^{-6}	1.3×10^{-8}	8.1×10^{-12}
31	$^5D_4 \rightarrow {}^7F_4$	$^7F_2 \rightarrow {}^5D_0$	862	2.2×10^{-5}	1.1×10^{-1}	4.2×10^{1}	5.2×10^{2}	0.0	1.1×10^{1}
32	$^5D_4 \rightarrow {}^7F_4$	$^7F_2 \rightarrow {}^5D_1$	-872	0.0	0.0	0.0	4.7×10^{2}	2.2	1.4×10^{-1}
33	$^5D_4 \rightarrow {}^7F_4$	$^7F_2 \rightarrow {}^5D_2$	-3328	1.2×10^{-29}	8.6×10^{-27}	3.1×10^{-24}	6.8×10^{-23}	1.8×10^{-25}	1.4×10^{-24}
34	$^5D_4 \rightarrow {}^7F_3$	$^7F_2 \rightarrow {}^5D_0$	-117	5.0×10^{-4}	3.2	2.6×10^{4}	3.0×10^{4}	0.0	6.4×10^{2}
35	$^5D_4 \rightarrow {}^7F_3$	$^7F_2 \rightarrow {}^5D_1$	-1851	0.0	0.0	0.0	1.8×10^{-4}	9.4×10^{-6}	5.3×10^{-10}
36	$^5D_4 \rightarrow {}^7F_3$	$^7F_2 \rightarrow {}^5D_2$	-4307	4.8×10^{-48}	9.9×10^{-45}	3.4×10^{-41}	6.8×10^{-41}	2.0×10^{-42}	2.2×10^{-51}
								$W_1 = \sum \omega =$	9.9×10^{4}

Table of content

Here is reported the tuning of the relative thermal sensitivity in a series of Eu-Tb mixed metal-organic framework luminescent thermometers. The sensitivity and the temperature range are modulated by an accurate control of the Eu/Tb ratio. Theorerical calculations highlight the chemical composition directly impacts the Tb-to-Eu energy transfer rate.

V.Trannoy, A. N. Carneiro Neto, C. D. S. Brites, L. D. Carlos, H. Serier-Brault*

Engineering of mixed Eu^{3+}/Tb^{3+} metal-organic frameworks luminescent thermometers with tunable sensitivity

ToC figure